Regular Article

Muhammad Yusvika, Aprianur Fajri, Tuswan Tuswan, Aditya Rio Prabowo*, Syamsul Hadi, Indri Yaningsih, Teguh Muttaqie and Fajar Budi Laksono

Numerical prediction of cavitation phenomena on marine vessel: Effect of the water environment profile on the propulsion performance

https://doi.org/10.1515/eng-2022-0034
received December 26, 2021; accepted March 15, 2022

Abstract: Energy-saving and emission reduction are crucial since shipping activity due to the global maritime trade has increased exponentially. Several agreements have been engaged to optimize ship energy efficiency composed of ship design and shipping operation planning. However, most up-to-date studies focused on speed and route optimization. The interaction analysis between speed and route efficiency below varied environmental conditions is limited. To attain energy and cost efficiency, a study of cavitation on the propeller that considers the ocean environmental condition will be discussed in this work. Although researchers have previously observed cavitation phenomena, the predictability of simulations is not yet such that problems can be eliminated. Since the multiphase flow of water and vapor is sensitive to environmental conditions, it leads to varying observation accuracy. Thus, the current paper proposes a new performance indicator of the ship propeller under cavitation predicted by computational fluid dynamics (CFD). CFD-based simulation to observe the propeller cavitation was used to model the Zwart cavitation and Kunz cavitation models under two turbulence models of K–ε and SST at different flow conditions and operating environments. Initial validation tests between experimental and numerical simulation show good agreement with a mean error of 4.7% in the Zwart model and 3.7% in the Kunz model, where the k–ε turbulence model provides an almost higher relative error. It is revealed from the result that the increase in temperature causes the rise in the cavitation problem. It is revealed from the result that the increase of temperature causes the increase in cavitation problem.

Keywords: energy efficiency, propeller, cavitation, water temperature, salinity, computational fluid dynamics

*** Corresponding author: Aditya Rio Prabowo,** Department of Mechanical Engineering, Universitas Sebelas Maret, Surakarta, Indonesia, e-mail: aditya@ft.uns.ac.id
Muhammad Yusvika, Aprianur Fajri, Syamsul Hadi, Indri Yaningsih: Department of Mechanical Engineering, Universitas Sebelas Maret, Surakarta, Indonesia
Tuswan Tuswan: Department of Naval Architecture, Universitas Diponegoro, Semarang, Indonesia
Teguh Muttaqie: Research Center of Hydrodynamics Technology, National Research and Innovation Agency of Indonesia (BRIN), Jakarta, Indonesia
Fajar Budi Laksono: Department of Research and Development, DTECH Inovasi Indonesia Co. Ltd., Salatiga, Indonesia

Abbreviations

CFD	computational fluid dynamics
EEDI	energy efficiency design index
GGI	general grid interface
GWP	global warming potential
IMO	International Maritime Organization
LFO	light fuel oil
LNG	liquefied natural gas
MRF	multiple reference frame
NSR	northern shipping route
PPCT	potsdam propeller test case
RANS	Reynolds-averaged Navier–Stokes
SCR	Suez canal route
SST	shear stress transport
SVA	Schiffbau-Versuchsanstalt

1 Introduction

Shipping is the most important mode of transportation for global commerce, accounting for about 90% of all global trade [1]. However, worldwide shipping is subjected to marine accident risk [2–5], and it is capable of a noteworthy increment in greenhouse gas emissions, which share almost 3% carbon dioxide (CO_2) and around

13% of total sulfur oxide emissions to the environment [6]. This issue might cause changing climate designs, rising ocean levels, and diminishing biodiversity. Based on the International Maritime Organization (IMO) [4] study, the CO_2 emissions from worldwide trade contain roughly 2.2% of the worldwide CO_2 emissions. Because of the increasing volume of global commerce, by 2050 pollution could rise by 150–250% if no action is taken [7].

The physical impacts of climate change have become one of the foremost fundamental issues nowadays. As shipping accounts for expanding CO_2 emissions, the Paris Agreement sets out a worldwide system to maintain a strategic distance from perilous climate change by restricting global warming to underneath 2°C and seeking after endeavors to constrain it to 1.5°C [8]. In 2011, IMO accomplished new rules to regulate the energy efficiency for ships to diminish emissions delivered by ocean-going vessels [9]. Based on those regulations, the vessels are committed to accomplishing a specific energy efficiency design index (EEDI) in order to extend energy efficacy and increase vessel cost-effectiveness.

Presently, there are generally three alternative ways to optimize energy efficiency. The first is from the point of view of a ship operation. The sailing speed and routes are optimized based on the relationship between fuel consumption and the vessel speed, related to the environmental conditions [10,11]. Then, the second is from the perspective of logistics. The economy of fleet navigation schedule and overall route planning is characterized to play down costs and outflow [12]. Third, optimizing the design and arrangement of hull shape and propulsion system based is the last option [13]. These three alternatives mean the industrial sector must consider long-term planning to adapt to new rules that comply with the EEDI to attain the shipping industry's vitality investment fund and emission reduction goals. Therefore, this article introduces technical analysis according to the perspective of shipping efficiency parameters based on the first and the third alternative strategy. This article attempts to combine the philosophy of ship design with ship operating environment, in which propulsion system performance will be related to environmental conditions.

Cavitation, a multiphase phenomenon, founded during ship operation, should be investigated accurately to predict the propulsion performance [14]. Cavitation can induce adverse effects such as performance loss, vibration, and noise [15]. This problem cannot be eliminated, but the ship only wastes energy without generating the required power if it is not controlled. Early recognition of these negative effects is essential in shipping navigation passing through the Arctic Ocean. The shipping activities may provide more disadvantages in the Arctic environment due to fossil fuel burned emissions. Arctic's viabilities have been the subject of numerous articles since the early decade [16–19]. So, it is crucial to account for the performance in propulsion design (e.g., by proper propeller design) and operations (control cavitation level) to prevent cavitation adverse effects and optimize fuel consumption and environmental conditions. With this issue, many engineering sectors are challenged to develop high-efficiency devices or energy alternatives. The designer is expected to solve these adverse effects to control the fuel cost of propeller efficiency and ensure compliance with the design requirement and green energy issue.

Cavitation may occur due to a low local static pressure combined with a high flow velocity, resulting in vapor pressure lower than the saturated water pressure of the liquid [20]. Propeller blades are arranged by several hydrofoil sections where the hydrofoil's upper surface has lower pressure than its bellow surface. This condition will remain to continue until the peak condition at a particular operation velocity. When the water pressure at the upper surface is lower than the saturated water pressure, liquid water will be transformed into the gaseous phase. This condition generates small vapor bubbles and then grows to a bigger diameter and then collects or coalesces to other macroscopic cavitation structures [21]. These cavitation bubbles cause the drop of thrust and torque produced by the propeller. Furthermore, when the cavitation bubbles arrive at the blade trailing edge or behind the propeller, they will receive higher pressure. This condition makes bubbles rapidly collapse and produce a high frequency of shock waves. The microjet causes erosion damage on the propeller surface [22].

The numerical simulations of cavitation on the propeller have been previously investigated. Morgut and Nobile [23] have simulated cavitation on a model propeller with three cavitation models of Zwart, Kunz, and full cavitation model using ANSYS CFX. The cavitating flow of the E779A and potsdam propeller test case (PPTC) propeller models was predicted using these three calibrated models. The research has successfully generated the optimum cavitation coefficient of each mass transfer model according to the operational conditions. Moreover, Helal et al. [24] have performed a cavitation study numerically on a model propeller INSEAN E779A using ANSYS Fluent with the transition-sensitive model (K–Kl–ω) and fully turbulence model (K–ε). The research was purposed to understand the existence of laminar and turbulent flow regimes. The results showed that both experiment and simulation had good agreement with experiments. The accomplishment of the two selected turbulence models indicated that (K–Kl–ω) was suitable for low rotational speed. Besides, conditions that had more existence of transition flow were appropriate

for K–ε. One of the challenges in investigating propeller cavitation is that the flow characteristic around the cavitating propeller contains multiscale flow physics, i.e., turbulence event, a phase change of the fluid, and unsteady loading. A comprehensive and detailed examination of the parameters influencing cavitation efficiency is needed for accurate performance prediction. With the case of different water properties, the result can be considered to enrich knowledge for the shipping industry in designing a propeller according to the needs and environmental conditions.

To address these issues, this work conducted a computational fluid dynamics (CFD)-based simulation to observe the propeller cavitation according to environmental conditions using ANSYS CFX. CEL expression language for CFX was used for modeling the Zwart cavitation model, which was known as the Zwart mass transfer model and the Kunz cavitation model [25,26]. The validation step was carried out with the Zwart and Kunz cavitation models and then was combined with two turbulence models of K–ε dan SST at three flow conditions and three operating environments. The structure of this article is constructed in sections as follows. Section 1 presents the introduction and objective of the study. A literature study on the Northern shipping route (NSR) commercial and environmental viability and previous cavitation studies related to temperature are reported in Section 2. Section 3 offers the mathematical model, and Section 4 reports the analysis of cavitation to its operating conditions. In the last, a few concluding remarks and summary are provided in Section 5.

2 Literature study

Exploration of the ocean is a big challenge for humans. There are regions blessed with tremendous and valuable common assets, e.g., renewable (wind, sun-based, wave) and non-renewable assets (oil, gas, minerals), which can advantage human life. It is attracting much interest in exploring and exploiting natural resources for human prosperity. The ocean must be managed equitably and sustainably because human activity can degrade and destroy the blue ecosystems.

2.1 Shipping in NSR and Suez canal route (SCR)

One of the extreme areas currently possible to conquer is the Arctic Ocean in the North Pole. Arctic shipping routes are the maritime route connected entirely of both east–west land and the Atlantic–Pacific Ocean. Located in the north polar of the Earth, it is characterized as a zone with a cold climate and secured by ice. This environment has been untouchable and nearly undisturbed by human activities for a long time. Recently, the route through parts of the Arctic is conceivable since the worldwide warming impact has made a more critical portion of the Arctic melting within the summer. Mainly it happens in March, as shown in Figure 1 [27].

Maritime container cargo contains an extraordinary potential request for the NSR shipping route, which is currently shipped through the SCR between East Asia and Northwest Europe (Figure 2). Vehicles are one of the foremost critical potential cargoes. Furthermore, other prospective cargoes, such as Murmansk gas condensate, Hammerfest liquefied natural gas (LNG), and Kirkenes iron ore, had already been commercially exported since 2009 to East Asia [28]. As global warming has retreated from the Arctic seas, NSR trade in East Asia and Northwest Europe lately has started to gain momentum, leading to the direct result of a 40% reduction in sailing distances relative to the SCR. The NSR is expected to take 19.3 days to transport, which is 35.4% quicker than the SCR (30.4 days).

The reduced effect of CO_2 pollution due to decreased distance is estimated between 13 and 35% for the NSR duty period of 105–225 days. This issue can entice the operators and shipowners based on the environmental benefits of shipping rather than the financial benefits [28]. Lindstad et al. [27] have investigated the combination of the emission obtained with the specified global warming potential (GWP) factors for the last 20 years. Twenty years of assessment based on relevancy to identify fuel and technology relations are used, resulting in the best climate impact reduction. It is compatible with the 2050 target of maintaining temperature stability at 2°C above pre-industrial levels.

It can be found that the positive values shown in Table 1 indicate a warming impact, and negative values have a cooling effect. Figure 3 exemplifies comparison data of trades through SCR and trades through NSR. This study uses Panamax dry bulkers for both shipping trades. The fuel options are light fuel oil (LFO), marine gas oil, and LNG. Each fuel option is divided into low power and high power. The bar shows that NSR yields the lowest cost compared to 18 USD/ton versus 29 USD/ton for NSR and SCR, respectively. However, compared to CO_2 equivalents (GWP_{20}), trades through NSR have a more significant climate effect per ton transported than trades through SCR. The LFO used in NSR trades, for example, is 65 kg CO_2-eq per ton transported, compared to 20 kg CO_2-eq in SCR trades.

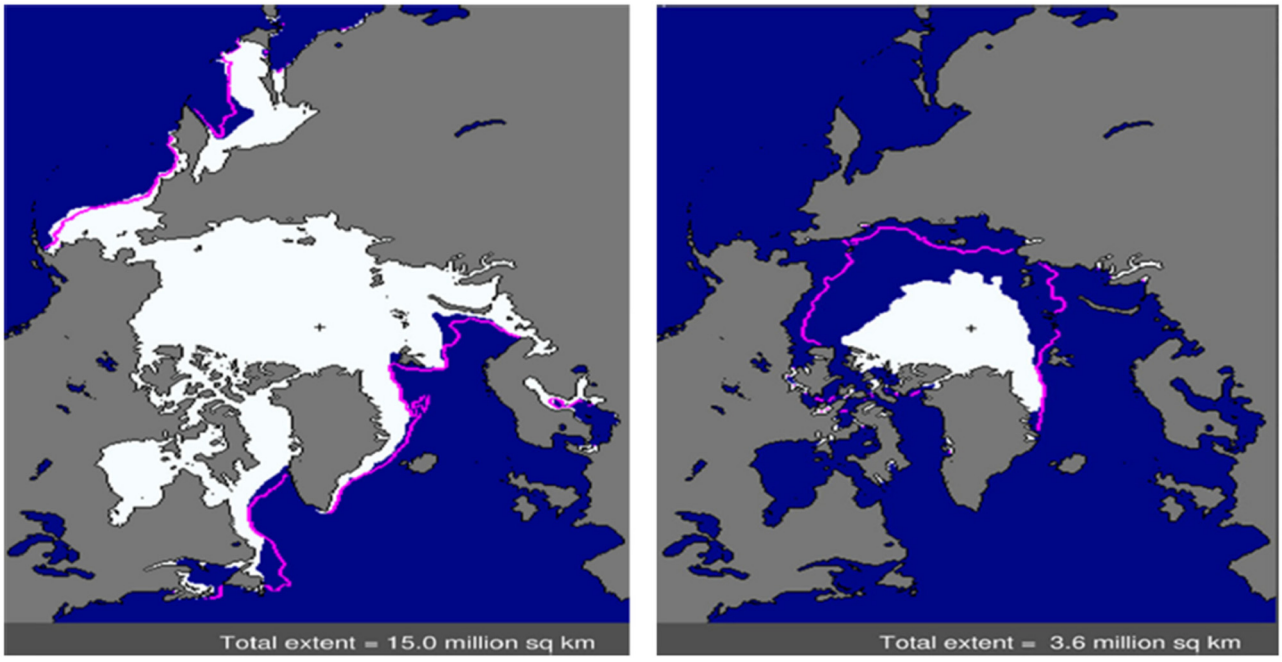

Figure 1: The total sea ice extent in March (left) and September 2012 (right). Purple lines reflect the median extent from 1979 to 2000 [29].

2.2 Water characteristic in ocean

The water characteristics in the ocean are dependent on the temperature. The natural water phase is liquid, but it could turn to a solid phase and gaseous/vapor phase determined from heat energy transferred by sunshine.

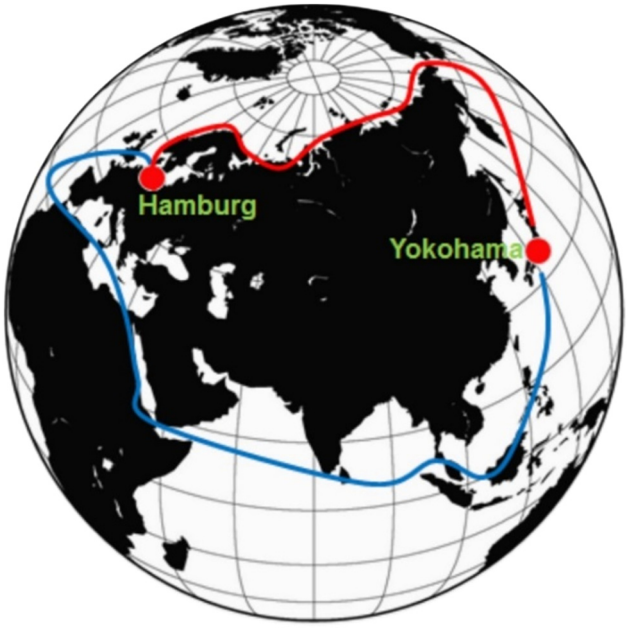

Figure 2: Comparison of shipping between NSR and SCR routes Hamburg to Yokohama [28].

Water has low thermal conductivity than air. It needs about four times the amount of energy to increase the temperature by 1°C, but it also means water is more difficult to release heat. Figure 4 depicts the heat maps of the ocean surface temperature of the Earth. The water near the equator has yellow until the red represents the warm zone and gets cold to the poles. The temperature of the world ocean surface imposes on Earth's climate and weather. The temperature of the ocean also varies according to the depth. There is a surface layer categorized up to 200 m deep, with the same temperature. Below the surface layer is a thermocline that reaches 1,000 m, colder from top to bottom. However, in this case, the study of ship operation is only on the surface. So, it is clear that the scope of ocean water in the following discussion means surface water of the ocean.

Besides temperature, the salinity of seawater is an exciting topic in oceanography. Seawater has different salinity levels influenced by temperature, pressure, conductivity, etc. The spectrum of practical salinity S_p is in the range $2 \leq S_p \leq 42$ [31]. The precise location of bulk material collection to prepare the standard seawater is not mentioned. The Standard Seawater Service issues guidance notes to ships collecting this bulk material, recommending that water be collected in deep water between longitudes 50 and 40°W during daylight hours. Millero et al. [32] created reference composition salinity S_R (or reference salinity for short) to be the best approximation in the mass fraction absolute salinity S_A of

Table 1: Potential of global warming per fuel type in kg-CO_2-equivalents/kg emission [27]

Type of emission	CO_2	BC	CH_4	CO	N_2O	NO_x	SO_2	OC
GWP_{20} world factor	1	1,200	85	5.40	264	−15.9	−141	−240
GWP_{20} world factor	1	6,200	85	5.40	264	−31.0	−47	−151
GWP_{100} world factor	1	345	30	1.80	265	−11.6	−38	−69
GWP_{100} world factor	1	1,700	30	1.80	265	−25.0	−13	−43

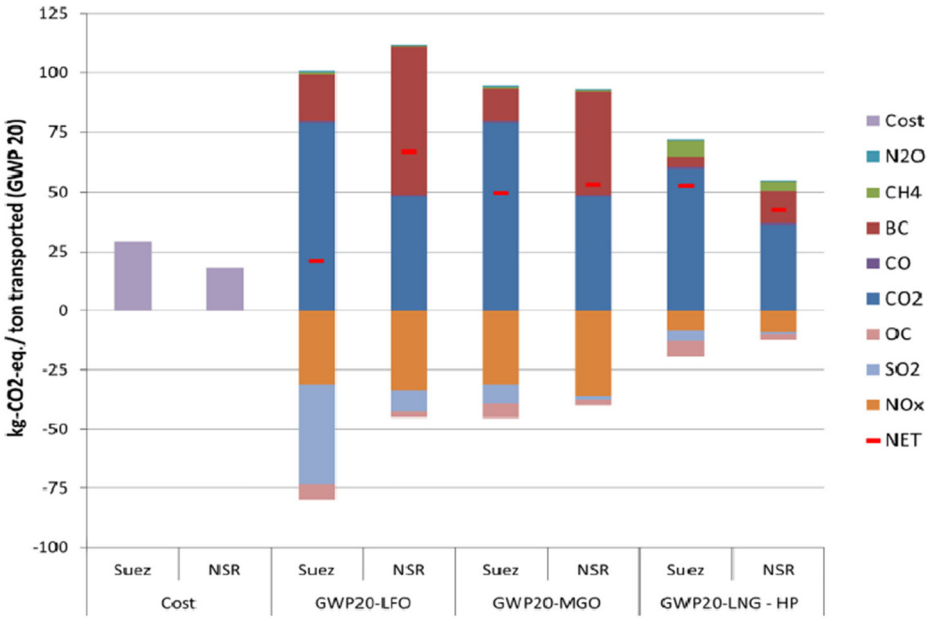

Figure 3: Suez versus NSR trades cost and kg CO_2 equivalent (GWP 20) per ton transported per fuel type [27].

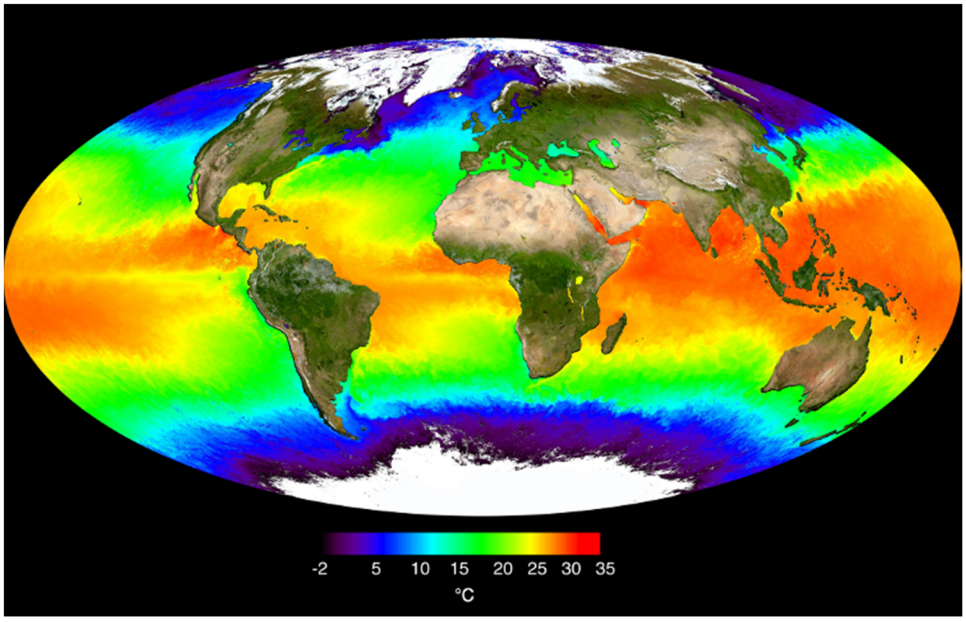

Figure 4: Sea surface temperature [30].

standard seawater. A seawater sample of reference composition whose practical salinity S_P is 35 has a reference salinity S_R of 35.16504 g kg^{-1} with absolute uncertainty is ±0.007 g kg^{-1}. The difference between reference and practical salinities may be attributed to the early method of calculating salinity by evaporating water from seawater and weighing the remaining solid content. This method also evaporated certain volatile elements, accounting for the majority of the 0.16504 g kg^{-1} salinity discrepancy.

Veronis measurements [33] revealed that after a temperature drops to −40°C, newly formed ice had a salinity of 10.16 g kg^{-1}. The ice salinity was as low as 5.64 g kg^{-1} after the temperature dropped to −16°C. Because of the salt solution, the salinity of ice reduces with age. It stays between the crystals during freezing since it is denser than ice and therefore leaches. Temperature readings have a minimum precision of 0.01°C. Ocean temperatures range from −1.9 to 30°C. The lower boundary is defined by the accumulation of ice. However, supercooled water with a temperature below the freezing point may be encountered. Water temperature in the surface layer of a closed sea can be higher than 30°C in extreme conditions.

Cavitation phenomena cannot be separated from the evaporation and condensation process. This process depends on the temperature, pressure, water properties, and other thermodynamics properties in its specific environment. The water boiling point marks phase transformation from liquid to gaseous. Both freshwater and seawater have different boiling points because of their properties. The boiling point of water is determined by saturation pressure. In the case of this study, the saturation pressure of water is differentiated by freshwater and seawater. Figure 5 shows the difference between the boiling point and saturation point of both seawater and freshwater.

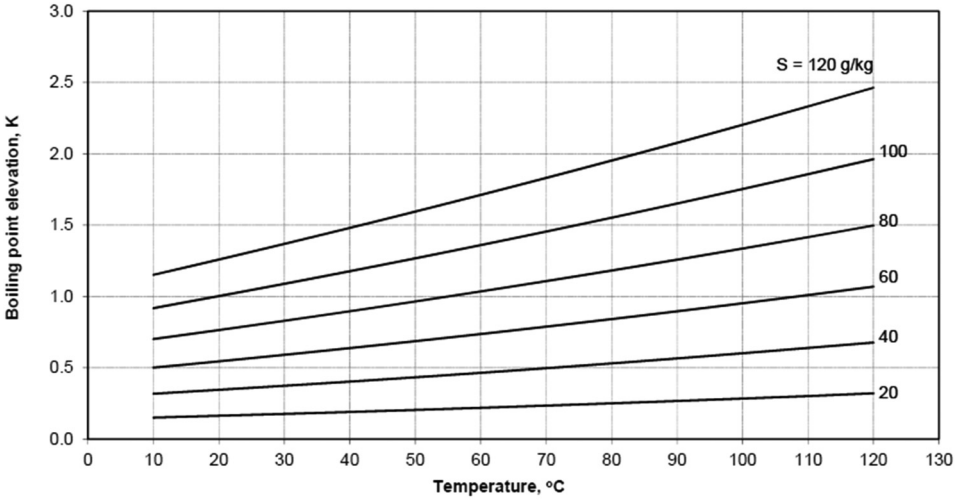

a

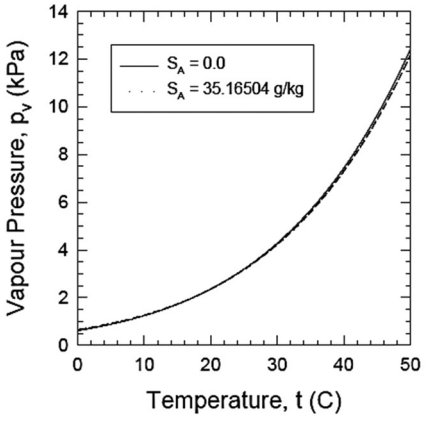

b

Figure 5: (a) Boiling point elevation of seawater based on salinity variation and (b) vapor pressure to temperature comparison relates to the salinity [34].

2.3 Previous cavitation research related to the temperature

Several researchers who studied the cavitation phenomena applied different techniques in approaching the cavitation phenomena. The effect of temperature on cavitation problems for various materials over a temperature range of 0–90°C has been studied by Plesset [35]. The findings showed that the optimum damage rate occurred at temperatures ranging from 40 to 50°C. Furthermore, Al-Arabi [36] used experimental observation to investigate the impact of water temperature on the efficiency and cavitation inception of a centrifugal pump. The section test was created to monitor the ratio of flow rate, suction pressure, rotational speed, and fluid temperature. The findings revealed that increasing the water temperature sped up cavitation and increased the net positive suction head.

Furthermore, an experimental test was conducted by Dular and Coutier-Delgosha [37] to research the effect of thermodynamics on a single cavitation bubble's growth and collapse. Their research focused on studying temperature changes in liquid environments. Experiments were conducted in a water-filled cylinder at room temperature and atmospheric pressure. The findings revealed that the growth of the bubble was caused by the extension of an initial air bubble. The experimental findings were compared to the "thermal delay" model's predictions. Temperature fluctuations are due to latent heat exchanges during the vaporization and condensation processes in this approach.

Tanaka [38] observed a centrifugal pump's thermodynamic cavitation efficiency experimentally in 2011. The findings found that cavitation performance with liquid nitrogen was superior to cavitation performance with cold water, and the expected temperature drop due to the thermodynamic effect decreased as the flow coefficient decreased. Furthermore, at the same flow coefficient, the predicted temperature drop attributable to the thermodynamic impact on the low cavitation condition was greater than on the high cavitation efficiency impeller. Kim and Song [39] conducted experimental research on the influence of temperature on the critical cavitation number in a turbopump inducer. According to the data, nondimensional thermal parameters increased the onset to a lower cavitation number and decreased cavitation rate. However, at 340 K and 5,000 rpm, the critical cavitation number and revolving cavitation onset were independent of the nondimensional thermal parameter for more than 0.540. Yusvika et al. [40] used CFD-based numerical simulation to simulate propeller cavitation based on water physical properties. The simulation effects of propeller output characteristics, propeller cavitation patterns, and fluid state were compared at observed temperatures ranging from 0 to 50°C. The cavitation phenomenon was modeled using the RANS system with several reference frames (MRF). The obtained results revealed a cavitation pattern occurring more vigorously as water temperature increased.

3 Mathematical model

3.1 Parameter of propeller performance

A parameter of propeller performances can be easily separated into open water and behind-hull properties, which have fundamental variations. This study observes the PPTC VP1304 propeller in open water by numerical simulation. The propeller thrust F (N) and torque Q (Nm) are expressed in a series of nondimensional characteristics, which are as follows [24]:

$$K_T = \frac{F}{\rho n^2 D^4}, \tag{1}$$

$$K_Q = \frac{Q}{\rho n^2 D^5}, \tag{2}$$

$$\eta = \frac{JK_T}{2\pi K_Q}, \tag{3}$$

$$J = \frac{V_A}{nD}, \tag{4}$$

where K_T and K_Q are the dimensionless coefficients of thrust and torque, D (m) is the diameter of the propeller, J is the advance coefficient, ρ (kg/m^3) is the fluid density, η is the open water efficiency, V_A (m/s) is the freestream fluid velocity, and n (rps) is the propeller rotational speed.

3.2 Calculation of cavitation event

Cavitation flow conditions were organized based on the cavitation number σ_n at the specified advance coefficient of testing. The pressure coefficient c_{p} and cavitation number σ_n can be defined as follows [24]:

$$\sigma_n = \frac{P_{\mathrm{Ref}} - P_{\mathrm{v}}}{1/2\rho(nD)^2}, \tag{5}$$

$$c_{\mathrm{p}} = \frac{P - P_{\mathrm{Ref}}}{1/2\rho(nD)^2}, \tag{6}$$

where P_{v} is the absolute vapor pressure, P is the local pressure, and P_{Ref} is the pressure used for reference.

Based on the theory of the cavitation inception criterion, cavitation will occur if $\sigma_n \leq c_p$.

3.3 Multiphase Reynolds-averaged Navier–Stokes (RANS) method

Cavitation flow analysis is gas-liquid two-phase mixture that combine water & water vapor into a single fluid mixed-phase state. The RANS equation can solve the multiphase flow if the combination of the two liquids is homogeneous. To approach turbulent flow, the RANS equation assumes that the fluid is incompressible and employs the eddy viscous model [23]. The following is the governing equation:

$$\bar{V} \cdot U = \dot{m}\left(\frac{1}{\rho_l} - \frac{1}{\rho_V}\right), \tag{7}$$

$$\frac{\partial(\rho u)}{\partial t} + \bar{V} \cdot (\rho\, UU) = -\bar{V}P_{\text{avg}} + \bar{V}\cdot[(\mu + \mu_t)\cdot(\bar{V}U + (\bar{V}U)^T)] + S, \tag{8}$$

$$\frac{\partial \gamma}{\partial t} + \bar{V} \cdot (\gamma\, U) = \frac{\dot{m}}{\rho_l}. \tag{9}$$

This equation represents the multiphase RANS equations. The volume continuity and momentum equation for the liquid–vapor mixture is shown on the left, and on the right, the volume fraction for the liquid phase. ρ_l and ρ_v are liquid and vapor density, respectively. P_{avg} represents the average pressure, U indicates the average velocity, S is the additional momentum, and γ indicates the water volume fraction. Then, α is the vapor volume fraction:

$$\gamma + \alpha = 1. \tag{10}$$

The multiphase flow is constructed from the mixing of liquid–vapor density as well as its dynamics viscosity. Each phase's density is expressed by a scalar volume fraction, which is as follows:

$$\rho_m = \alpha\rho_V + (1 - \alpha)\rho_L, \tag{11}$$

equal to:

$$\mu_m = \alpha\mu_V + (1 - \alpha)\mu_L, \tag{12}$$

where ρ_m represents the mixture density, $\dot{m}$ is the interphase transfer rate due to cavitation, and μ_m is the dynamic viscosity of the mixture. Furthermore, the eddy viscous turbulent model was used to close the governing equation model and treat the two liquid–vapor phases as one phase. The standard fully k–ε turbulence model and shear stress transport (SST) turbulence models were used for each simulation in the test case. Meanwhile, for the observation part, only the SST turbulence model was used because it considers the validation in the test case, which has superior accuracy with the SST turbulence model to k–ε.

3.4 Bubble cavity inception process and mass transfer model

The first stage of cavitation begins with the formation of bubbles. It assumes that the cavitation bubble is a homogeneous phase and analyzes only one bubble during the flows, despite it being impossible in practice. The bubbles grow larger following its pressure at the local area. The Rayleigh–Plesset equation is used to model bubble growth. It represents the increasing diameter of bubbles in a fluid as a time function. The equation measures growth in a single bubble when assuming no thermodynamic flow or temperature decrease from bubble initiation to collapse. For test and observation scenarios, the equation has been used as a mass transfer model in CFX, and it is as follows [41]:

$$R_B\frac{d^2R_B}{dt^2} + \frac{3}{2}\left(\frac{dR_B}{dt}\right)^2 + \frac{2\sigma}{R_B} = \frac{P_v - P}{\rho_l}, \tag{13}$$

where R_B represents the bubble radius, P_v indicates the pressure of the bubble at the fluid reference temperature, and P is the pressure around the bubble. ρ_l and 2σ reflect the fluid density and surface tension coefficient of water vapor and fluid, respectively. When the second derivative is removed, the equation is reduced to:

$$\frac{dR_B}{dt} = \sqrt{\frac{2(P_v - P)}{3\rho_l}}. \tag{14}$$

The rate of bubble volume growth is described as follows:

$$\frac{dV_B}{dt} = \frac{d}{dt}\left(\frac{4}{3}\pi R_B^3\right) = 4\pi R_B^2\sqrt{\frac{2(P_v - P)}{3\rho_l}}, \tag{15}$$

while the rate of change in mass of the bubble can be described as follows:

$$\frac{dm_B}{dt} = \rho_v\frac{dV_B}{dt} = 4\pi R_B^3\rho_v\sqrt{\frac{2(P_v - P)}{3\rho_l}}. \tag{16}$$

If the number of bubbles per unit volume is defined by N_B, then the equation for the bubble vapor volume fraction α is

$$\alpha = V_B N_B = 4\pi R_B^3 N_B . \quad (17)$$

The total mass transfer rate per volume is then set as follows:

$$\dot{m} = N_B \frac{dm_B}{dt} = \frac{3\alpha\rho_v}{R_B}\sqrt{\frac{2(P_v - P)}{3\rho_l}} . \quad (18)$$

As the vaporization process occurs, the bubble volume fraction increases with increasing bubble diameter, and the nucleation density decreases. As a result, the volume fraction of water vapor produced during vaporization is a feature of $r_n(1 - \alpha)$. The rate of vaporization and condensation bubble formation can be described as follows:

$$\dot{m} = \begin{cases} F_v \dfrac{3r_n(1-\alpha)\rho_v}{R_B}\sqrt{\dfrac{2(P_v - P)}{3\rho_l}} & \text{if } P < P_v, \\ F_c \dfrac{3\alpha\rho_v}{R_B}\sqrt{\dfrac{2(P_v - P)}{3\rho_l}} & \text{if } P > P_v, \end{cases} \quad (19)$$

where r_n represents the nucleation site of the vapor volume fraction, F_v and F_c reflect the empirical calibration coefficient of evaporation and condensation, respectively, and α represents the vapor volume fraction. The following model parameters have been shown to be effective for a wide range of fluids: $R_B = 10^{-6}m$, $r_n = 5 \times 10^{-4}$, $F_v = 50$, $F_c = 0.01$. This model of cavitation flow is known as the Zwart mass transfer model or the Zwart cavitation model.

3.5 Kunz cavitation model

This mass transfer model parameter is set up in two ways to build $\dot{m}^+$ and destroy $\dot{m}^-$ of liquid. The liquid-to-vapor transition is measured as a function of how much pressure is below the vapor pressure. Otherwise, the conversion of vapor to liquid is dependent on a third-order polynomial function of volume fraction, C. The specific mass transfer rate is denoted by the formula $m = (m^+) + (m^-)$.

$$\dot{m}^+ = \frac{C_{prod}\rho_v \gamma^2(1-\gamma)}{t_\infty}, \quad (20)$$

$$\dot{m}^- = \frac{C_{dest}\rho_v \gamma_{min}(0, P - P_v)}{(1/2\rho_l U_\infty^2)t_\infty}, \quad (21)$$

where $t_\infty = L/U$ denotes the mean flow time scale, U_∞ (m/s) represents the freestream velocity, L is the characteristic length scale, and C_{dest} and C_{prod} are two empirical coefficients, respectively, where $C_{dest} = 100$ and $C_{prod} = 100$ are assumed.

3.6 Thermodynamic parameter

The thermodynamic parameter is known as the change in water temperature and is used to calculate the behavior of bubble dynamics. Thermodynamic behavior $\sum$ can be denoted as [42]:

$$\sum = \frac{\rho_v^2 L^2}{\rho_l^2 C_{p,v} T \sqrt{\frac{C_{p,l}}{\rho_l C_{p,v}}}}, \quad (22)$$

where L denotes the latent heat of vaporization, ρ represents the density, the specific heat at constant pressure is indicated by C_p, and T is the temperature of the liquid.

4 Numerical modeling

4.1 The cavitation tests conducted in the Schiffbau-Versuchsanstalt (SVA) potsdam

In this work, the cavitation experiments were conducted using the cavitation tunnel K15A (Kempf and Remmers)

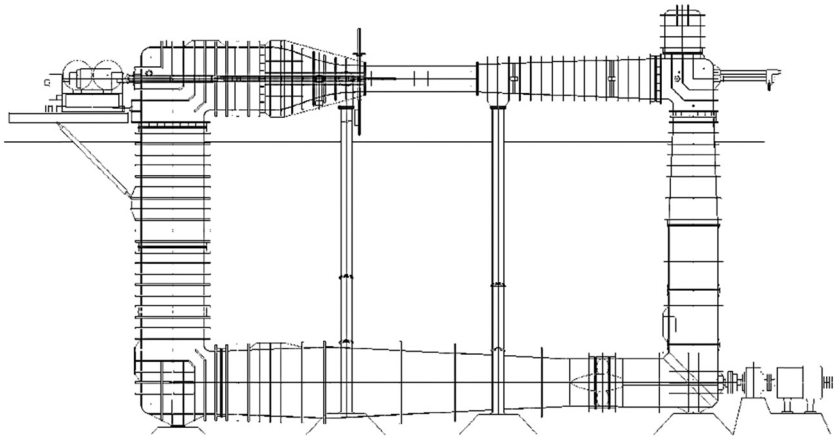

Figure 6: Cavitation tunnel in the potsdam cavitation test [43].

of the SVA Potsdam [43]. A dimension with a length of 2593.5 mm and a cross-section of 850 × 850 mm was used for cavitation observation tests. Figure 6 depicts the cavitation tunnel in the potsdam cavitation test.

Throughout measurement, the propeller was mounted according to the configuration shown in Figure 6, with a 12° inclination of the propeller toward the inflow direction or the X-axis. In this case, the propeller in an inhomogeneous environment is powered by the cavitation tunnel's homogeneous inflow. Tangential velocities work on one side of the propeller against and on the other side with the direction of blade rotation. Figure 7 shows the cavitation test section.

For the simulation, this study has slight differences compared to the testing model. The simplification technique is applied, which only involves a propeller without a hub and shaft to achieve optimal element mesh due to resource limitation of computer capabilities. This method was valid because the hub behind the propeller would not disrupt the inflow. This technique was also used in simulation techniques by Morgut et al. [44], as shown in Figure 8.

The inflow velocity in the numerical calculations can be determined with the advance coefficient. The pressure level in the numerical calculations can be resolved with the cavitation number. All evaluations shall be conducted with the propeller being in the zero-degree position. The origin of the geometry corresponds to the propeller plane position (x = 0 m). The calculations must be carried out according to the thrust identity (KT values are provided, non-cavitating), with the inflow velocity free to alter. The revolution rate is kept constant as it is used to define the cavitation number.

4.2 Propeller model and test case scenario

With the aim of testing and validation, SVA Potsdam developed a PPTC model VP1304 propeller model. The propeller consists of five blades with a controllable pitch propeller and a right-handed direction of rotation, as shown in Figure 9. The experimental data and geometries are available for viewing on the company website [43]. The VP1304 model was used in previous research for numerical simulation and validation results. Instead of experimental analysis, numerical simulation of the propeller output under cavitating flows using CFD-based software has been a good choice.

The simulation began with the simulation of the cavitating flow for validation purposes under existing conditions and then continued with the observational scenario. Fluid properties of water and vapor are set according to the water condition in the experimental testing tank. The physical properties used in numerical simulations are assumed that water is freshwater and seawater. The saturation vapor pressure is a representation of the reference temperature. As shown in Table 2, this section consists of three operating cases.

Table 2 displays the operational parameter, i.e., the observation scenario as a case to be studied. The simulation uses J, σ_n, and n as fixed parameters, while other parameters are temperature dependent and are the most important to observe. Water temperature varies at 1, 10, and 20°C. The current cavitating flow for the test case is subjected to fluid properties at 22, 21.9, and 23.2°C. New water material at specified water temperature is set to define water and vapor's thermodynamic and transport properties. Furthermore, Table 3 offers a comprehensive description of the fluid's properties. Using the CalcSteam online calculator, all fluids are measured based on the water temperature. In Table 3, all parameters with different temperatures are shown, with the new outlet boundary conditions as the static

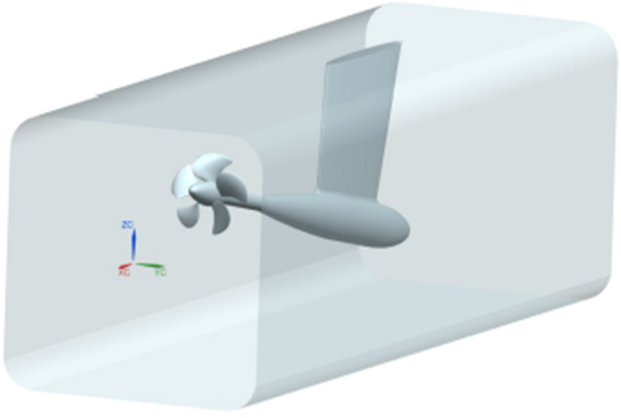

Figure 7: Cavitation test section [43].

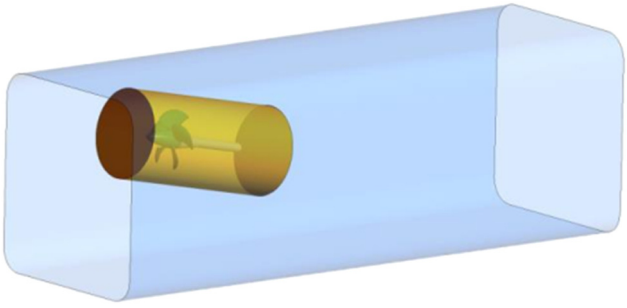

Figure 8: Morgut et al. simulation model [44].

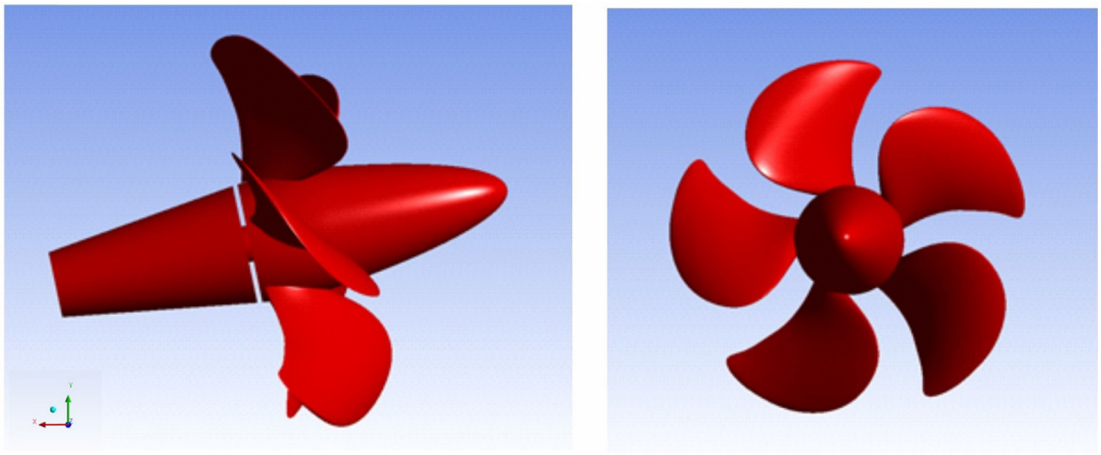

Figure 9: 3D images of the Potsdam Test Case Propeller (PPTC1) VP1304 model.

pressure choice determined using the equation of cavitation number.

4.3 Model validation

For validation purposes, the design of the computational domain used for the simulation test under consideration is a cylinder, as shown in Figure 10. The diameter D of the VP1304 propeller is 250 mm. The width and length of the rotating domain are 270 and 300 mm, respectively. The test section has an area of 850 mm × 850 mm perpendicular to the flow direction. The fixed domain is extended to 2593.5 mm overall. The simulations were run in 3D and assumed a steady-state condition. Because of the open water conditions, the propeller moved forward in a homogeneous uniform flow. The multiple reference frame (MRF) method was used to simulate propeller rotation, with the rotational speed remaining constant at $n = 20$ rps. The domain is divided into two parts: a rotating part and a fixed part. The MRF method analyzes the rotating domain in relation to other domains, while the general grid interface (GGI) method approximates a continuous surface [45].

Table 3: A summary of the parameters in different temperatures

Parameters	Unit	1°C	10°C	20°C
P_v	bar	0.6571^{-2}	1.228^{-2}	2.339^{-2}
ρ_l	kg/m^3	999.852	999.654	998.161
ρ_v	kg/m^3	5.196^{-3}	9.406^{-3}	17.310^{-3}
μ_l	Pa· s	1.731^{-3}	1.306^{-3}	1.001^{-3}
μ_v	Pa·s	9.239^{-6}	9.461^{-6}	9.727^{-6}
h_l	kJ/kg	4.177	42.021	83.919
h_v	kJ/kg	2502.729	2519.229	2537.469
s_l	kJ/kg K	0.152^{-1}	1.511^{-1}	2.96^{-1}
s_v	kJ/kg K	9.129	8.899	8.667
$C_{p,l}$	kJ/kg K	4.216	4.195	4.185
$C_{p,v}$	kJ/kg K	1.423	1.896	1.905
α_l	W/m K	0.563	0.579	0.598
α_v	W/m K	1.712^{-2}	1.762^{-2}	1.822^{-2}

P_v denotes fluid and vapor pressure at reference temperatures, respectively; ρ_l is the water density; ρ_v represents the vapor density; μ_l and μ_v are dynamic viscosity of water and vapor, respectively; h_l, h_v, s_l, and s_v are thermodynamic parameters consisting of enthalpy and entropy of liquid and vapor, respectively; $C_{p,l}$ and $C_{p,v}$ denote the isobaric heat capacity of fluids; and α_l and $\alpha_v$represent thermal conductivity of water and vapor.

Table 2: Operational parameters

Parameters	Symbol	Unit	Case 1	Case 2	Case 3
Advance coefficient	J	—	1.019	1.269	1.408
Cavitation number	σ_n	—	2.024	1.424	2.000
Rotational speed	n	rps	20	20	20
Saturated pressure	P_v	Pa	2,643	2,626	2,904
Water temperature	T	°C	22.0	21.9	23.2
Water density	ρ	kg/m^3	997.780	997.800	997.410

Table 4: Numerical cavitation test setup

Parameter	Type	Setting
Inlet domain	Normal speed	Case 1, $u = 5.095$ m/s Case 2, $u = 6.345$ m/s Case 3, $u = 7.040$ m/s
Inlet heat transfer	Static temperature	T (°C)
Turbulent intensity	Low intensity	1%
Outlet pressure	Static pressure	$P_{out} = P_{ref}$
Fluid definition	Volume fraction	Water (1) and vapor (0)
Rotating domain	Rotational speed	20 rps
Multiphase	Mixture	Homogeneous
Heat transfer	Homogenous	Total energy
Turbulent	SST	Automatic wall function
Mass transfer	Cavitation	Rayleigh–Plesset
Nucleation	Mean diameter	2×10^{-6}
Saturation vapor	Pressure	P_v

The single rotational speed of the water was applied to obtain the value of advance coefficient J and cavitation number σ_n. The advance coefficient J was used to measure the inlet velocity. The turbulent pressure boundary on the inlet was set at 1%. The pressure outlet for each run was determined using the cavitation number σ_n equation. The pressure outlet was $P_{out} = P_{ref}$ with a static pressure option for all simulations. The free slip boundary condition was added to the domain's outer boundary, while the propeller or solid surface was set with a no-slip boundary condition. The domain motion on the rotating domain was set to rotate with angular velocity. Furthermore, the stationary motion was applied. First, SST with automated wall treatment was used to influence the turbulent transition flow. In this work, the standard k–ε is applied in the next step for the full turbulence model with a scalable wall function. The Rayleigh–Plesset equation was used to describe cavitation bubble growth. Table 4 shows additional configuration parameters.

4.4 Meshing strategy

The chosen meshing method is an unstructured grid and hybrid mesh, which provides high precision. The rotating and fixed domain parts of the domain were segregated in this analysis. The mesh was created with CFX's solver mesh (Figure 11). The rotating domain was initialized automatically, and the fixed domain was defined using the tetrahedron method. The CFX solver will join the rotating and fixed interfaces meshing method using a simplified grid interface (GGI). The mesh sizing with the body of influence selection to approach more precision for the critical segment was used to reduce the number of mesh elements and maximize the mesh density. Then, 11 layers with inflation on the propeller surface to obtain the viscous effect as the turbulent boundary layer were placed. For all propeller surfaces, all meshes have the same y^+ value of approximately 10. The following equation can be used to calculate the y^+ value [24]:

$$y^+ = \sqrt{\frac{\frac{\tau_w}{\rho_l} y}{\nu}}, \tag{23}$$

where ν denotes the kinematic viscosity of the fluid, τ_w represents the shear stress at the wall, ρ_l denotes the density of the water, and y represents the normal distance from the wall.

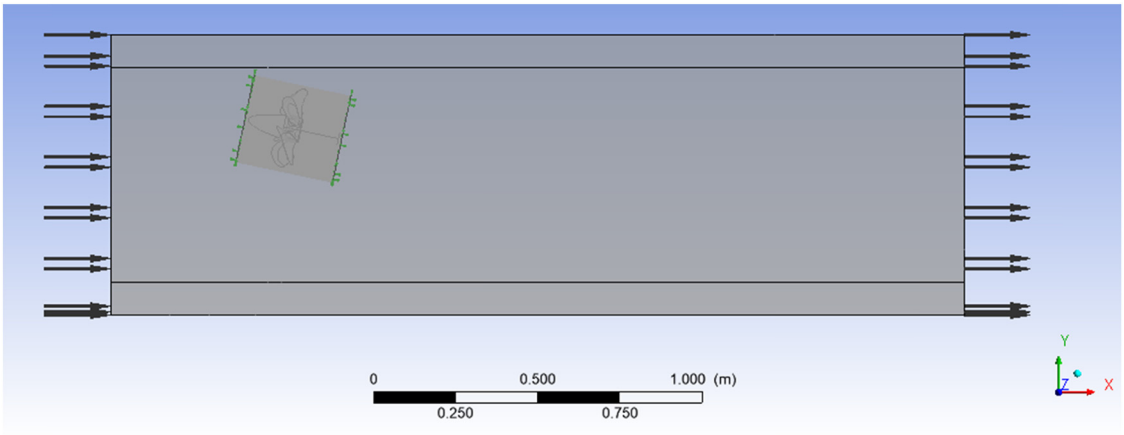

Figure 10: Design of computational domain.

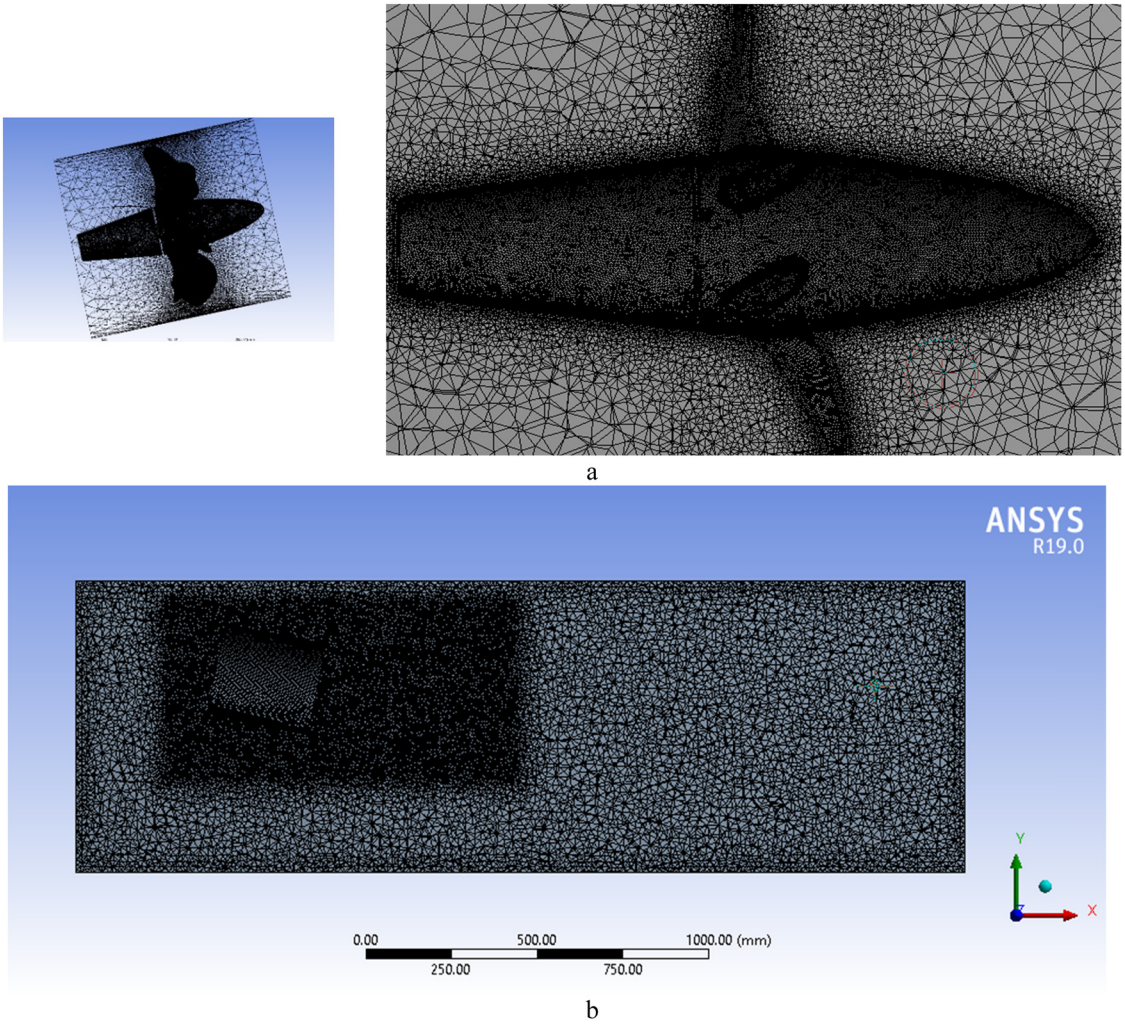

Figure 11: Mesh generated in Ansys program: (a) mesh interface for the rotating domain; and (b) mesh interface for a fixed domain.

4.5 Solution and solver setting

The CFD platform ANSYS CFX 19 was used for simulation, which offers solutions for three-dimensional viscous scenarios. The propeller cavitation simulation was performed under the assumption of steady-state conditions. The "upwind" advection scheme was added to the turbulent numerical high-resolution transport equation. The dynamic control model used the velocity–pressure coupling and multiphase control models.

4.6 Verification and validation tests

Verification and validation tests are conducted to investigate the effects of fluid properties and temperature effects on the cavitation process. Following that, the effects of propeller output at three operating conditions: (J = 1.019, σ_n = 2.024), (J = 1.269, σ_n = 1.424), and (J = 1.408, σ_n = 2.000) are compared. The output of thrust and torque coefficient is calculated in this section using CFX results by comparing two turbulence models of k–ε and SST. Following that, in each case, all nondimensional coefficients of output (K_T and K_Q) are determined. The Zwart cavitation and Kunz Cavitation models' validation results under various operating conditions are shown in Tables 5 and 6, respectively.

Furthermore, the validation stage was extended by performing a mesh dependence analysis to achieve optimum meshing. Table 7 displays the meshing information for the rotating and fixed domains depending on the number of elements. The optimum meshing value was calculated by taking simulation time and data error precision into account. It can be found that the longer the running time, the more the total of mesh elements. The result of K_T value was

Table 5: Comparison results between experimental test and numerical simulation using the Zwart cavitation model

J	σ_n	Experiment		Simulation				Relative error (%)			
		K_T	K_Q	K_T		10 K_Q		K_T		K_Q	
				k–ε	SST	k–ε	SST	k–ε	SST	k–ε	SST
1.019	2.024	0.373	0.940	0.384	0.383	0.989	0.975	3.0	2.8	5.2	3.7
1.269	1.424	0.206	0.730	0.230	0.209	0.691	0.701	11.5	1.3	−5.3	−3.9
1.408	2.000	0.136	0.560	0.145	0.144	0.580	0.584	6.7	5.6	3.6	4.3

Table 6: Comparison results between experimental test and numerical simulation using the Kunz cavitation model

J	σ_n	Experiment		Simulation				Relative error (%)			
		K_T	K_Q	K_T		$10K_Q$		K_T		K_Q	
				k–ε	SST	k–ε	SST	k–ε	SST	k–ε	SST
1.019	2.024	0.373	0.940	0.351	0.352	0.897	0.924	−5.7	−5.5	−4.6	−1.7
1.269	1.424	0.206	0.730	0.200	0.198	0.683	0.700	−3.3	−3.9	−6.4	−4.0
1.408	2.000	0.136	0.560	0.132	0.132	0.541	0.529	−3.1	−2.8	−3.5	−3.5

Table 7: Mesh dependency study of Case 1 using the Zwart model (J = 1.019, σ_n = 2.024)

Mesh case	Element in rotating domain	Element in a fixed domain	K_T	Error (%)
Coarse	5,754,160	1,159,145	0.129	37.27
Medium	7,301,426	2,452,774	0.139	12.32
Fine	9,440,483	3,780,050	0.144	5.60

determined using Case 3 at the existing temperature, and the error value was determined by comparing the simulation results to the experimental data collected in SVA potsdam's cavitation tunnel [24].

There are inconsistencies in the results of simulation data in experiments of both cavitation models with variable errors in Tables 5 and 6, assuming steady state and heat transfer during the process are set with total energy. The comparison of numerical results shows that the predicted cavitation at the three operating conditions by both turbulence models is in good agreement with the corresponding experimental results. For the K_T and K_Q coefficients, the agreement between predicted results based on both numerical and experiments is good. The relative error value differs between k–ε and SST turbulence models, with the k–ε turbulence model providing an almost higher relative error, while SST produces

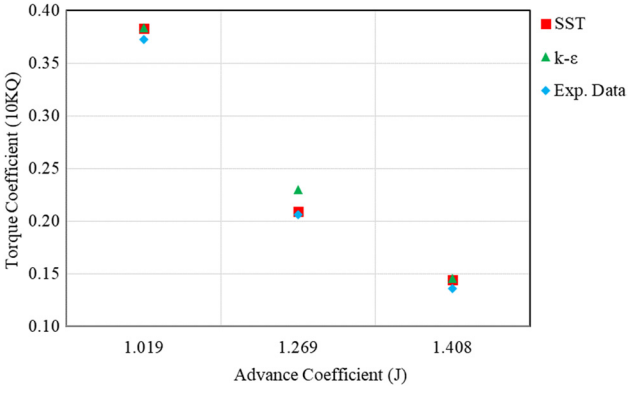

Figure 12: Numerical results of thrust coefficient (K_T) of Zwart Cavitation Model.

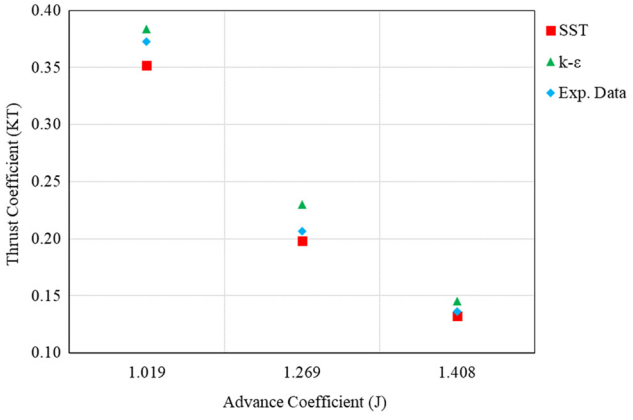

Figure 13: Numerical results of torque coefficient ($10K_Q$) of the Zwart cavitation model.

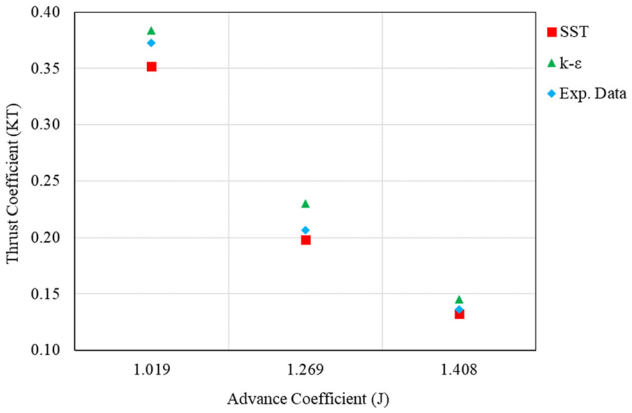

Figure 14: Numerical results of thrust coefficient (K_T) of the Kunz cavitation model.

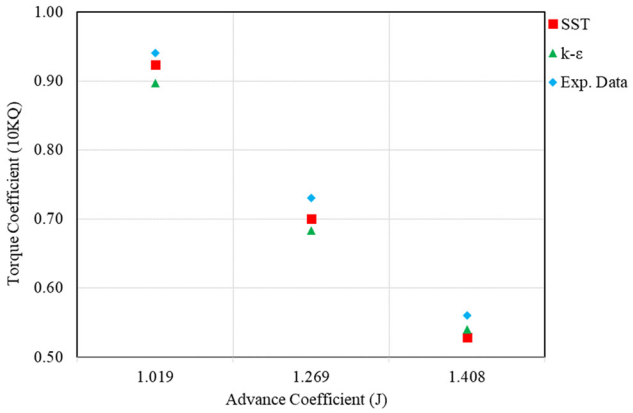

Figure 15: Numerical results of torque coefficient ($10K_Q$) of the Kunz cavitation model.

more variable results. Based on the simulation results in Tables 5 and 6, the SST turbulence model is superior to the k–ε turbulence model for modeling cavitation. As a result, the simulation in the second stage was entirely based on SST turbulence models. Figures 12–15 provide a comparative graphic of K_T and K_Q values based on observations and simulations of various turbulence models.

5 Observation of simulation results

The influence of simulation results on propeller performance under different operational conditions is discussed in this section. Tables 8–10 compare thrust and torque coefficients and the relative error under three different case scenarios. The torque and thrust coefficients under

Table 8: Comparison of coefficient of thrust and torque for case 1 ($J = 1.019$, $\sigma_n = 2.024$)

Temperature (°C)	K_T	ΔK_T (%) to K_T at 22°C	$10K_Q$	ΔK_Q (%) to K_T at 22°C
Existing temperature (22.0)	0.383	—	0.097	—
1	0.390	1.744	0.102	5.034
10	0.387	1.147	0.099	1.138
20	0.384	0.370	0.098	0.454

Table 9: Comparison of coefficient of thrust and torque for case 2 ($J = 1.269$, $\sigma_n = 1.424$)

Temperature (°C)	K_T	ΔK_T (%) to K_T at 21.9°C	$10K_Q$	ΔK_Q (%) to K_T at 21.9°C
Existing temperature (21.9)	0.209	—	0.070	—
1	0.217	3.910	0.072	2.837
10	0.212	1.451	0.071	1.907
20	0.209	0.158	0.070	0.175

Table 10: Comparison of coefficient of thrust and torque for case 3 ($J = 1.408$, $\sigma_n = 2.000$)

Temperature (°C)	K_T	ΔK_T (%) to K_T at 23.2°C	$10K_Q$	ΔK_Q (%) to K_T at 23.2°C
Existing temperature (23.2)	0.144	—	0.058	—
1	0.147	2.154	0.060	1.949
10	0.146	1.610	0.059	0.775
20	0.144	0.419	0.059	0.427

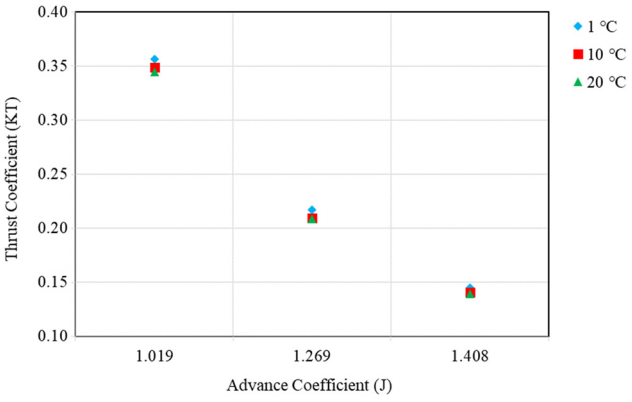

Figure 16: Numerical results of thrust coefficient (K_T) under variation of advance coefficient.

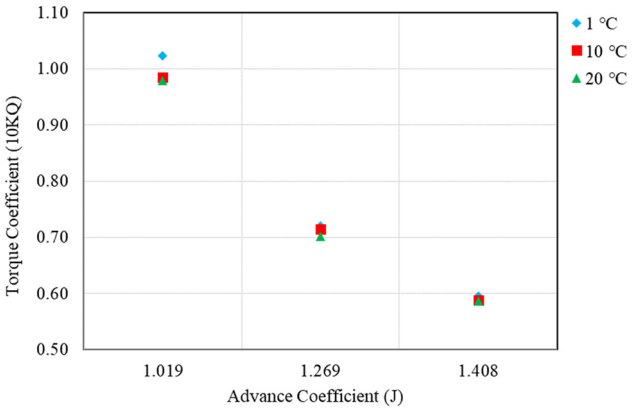

Figure 17: Numerical result of torque coefficient ($10K_Q$) under variation of advance coefficient.

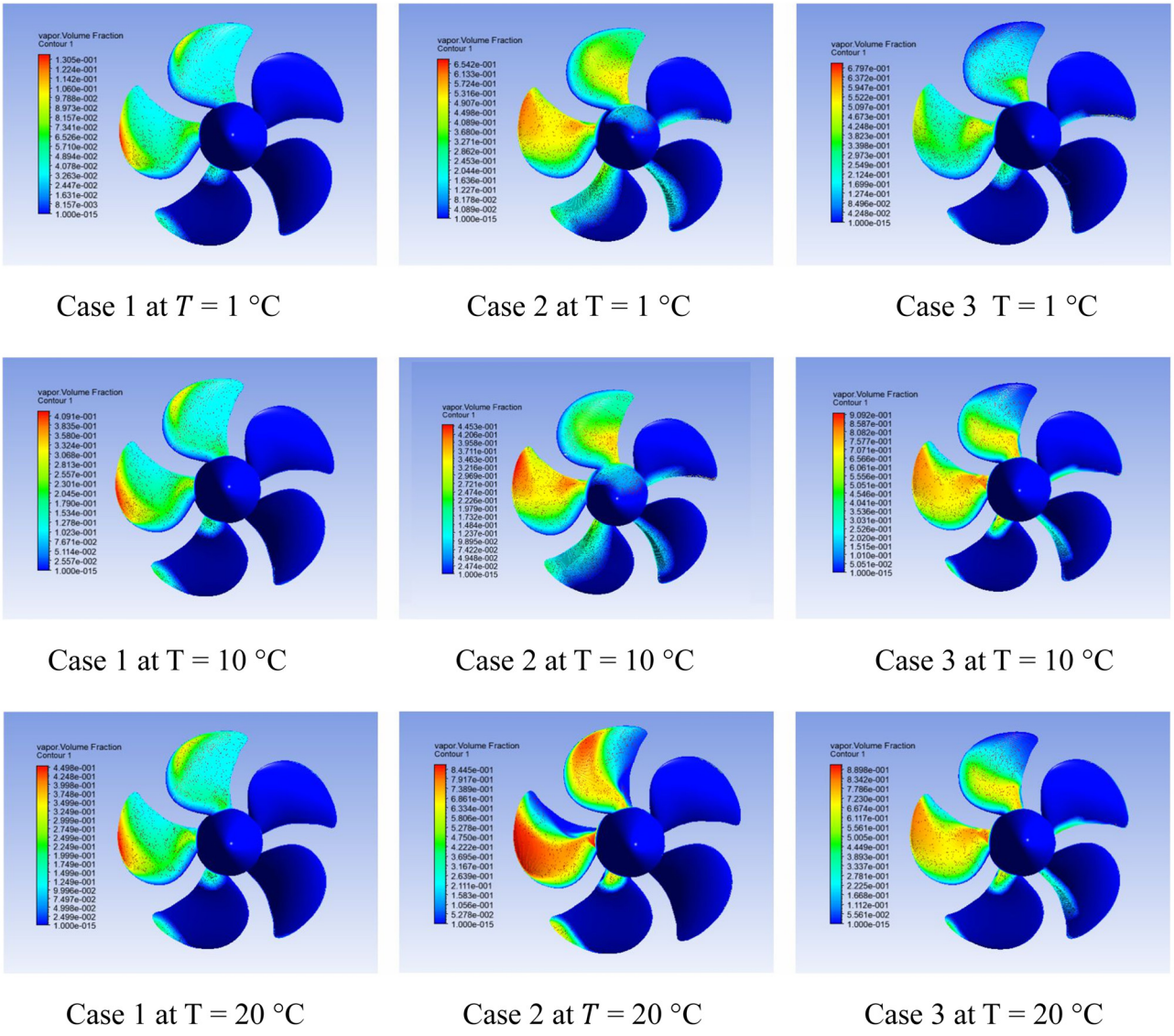

Figure 18: Vapor volume fraction contour of the suction side for three different cases and conditions. Results are obtained at a vapor volume fraction of 0.4.

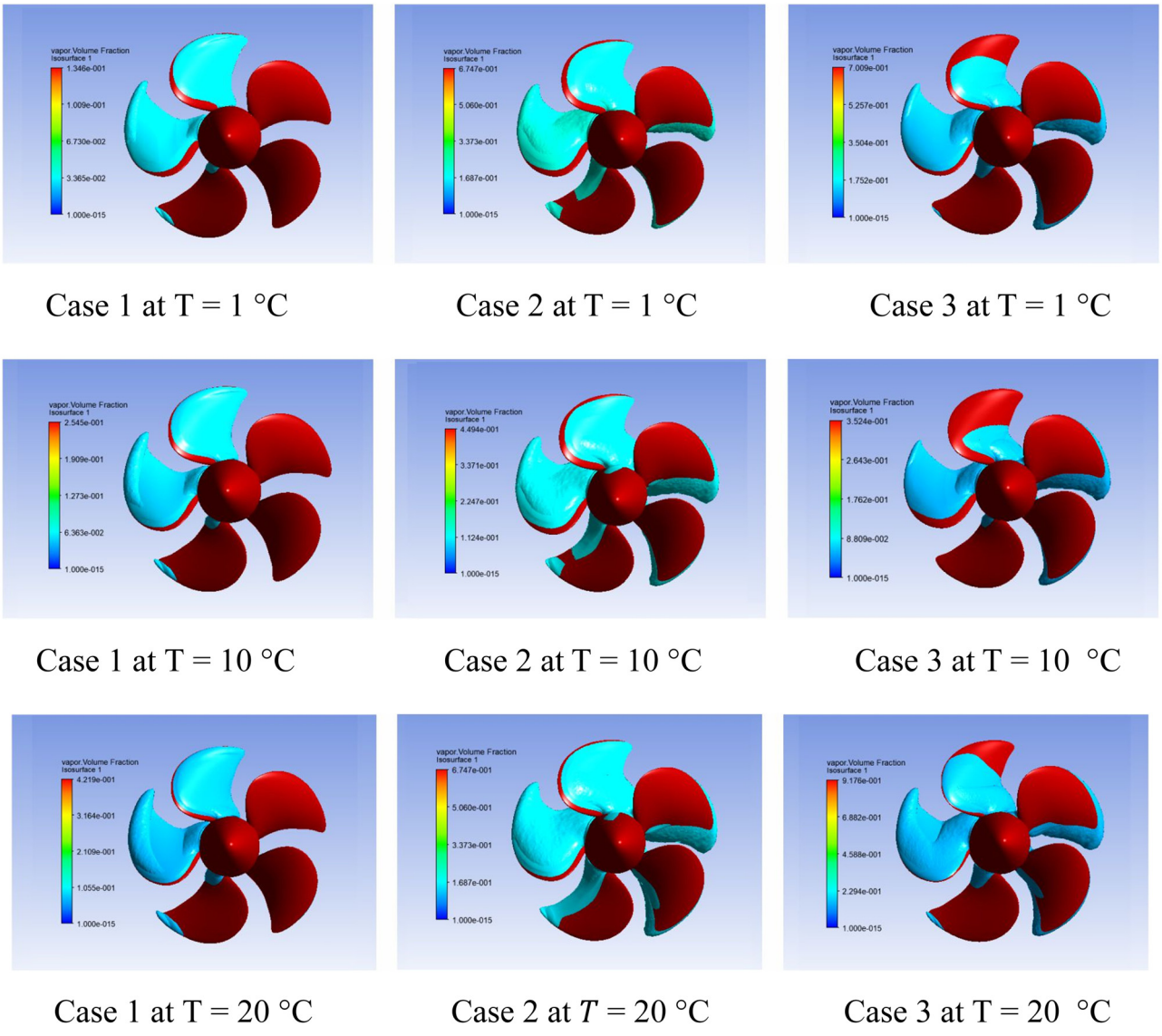

Figure 19: Isosurface cavitation of the suction side for three different cases and conditions. Results are obtained at a vapor volume fraction of 0.4.

three temperature values are compared to the value calculated in the existing temperature. To illustrate in more detail, Figures 16 and 17 depict a schematic comparison between the advance coefficient (J) and the performance coefficient of K_T and K_Q. Based on the result in Tables 8–10, it is understood that at the temperature of 1°C, the torque and thrust coefficient values have the highest difference compared to the data in normal temperature conditions; this occurs in all cases (Cases 1–3). It can be seen in the deviation percentage in all evaluated cases that the higher the temperature, the higher the deviation occurs. With increasing temperature, it can be realized that the propeller performances experience a decreasing trend. It means that the rising cavitation pattern is defined by decreased propeller output as temperature rises. The gap in ambient temperature significantly impacts propeller performance under cavitation conditions. Moreover, comparing the performance of all evaluated cases, the cavitation that occurs in case 1 is the most aggressive.

The findings are consistent with Al-Arabi [36], who investigated the cavitation in the centrifugal pumps at various water temperatures. It can be found that the decrease in the pump head is proportional to the rise in temperature. Moreover, Dular and Petkovšek [46] investigated liquid nitrogen and water cavitation at temperatures ranging from 20 to 90°C. It is found that the erosion rate was found to be proportional to the rise in water temperature in tests. Moreover, Plesset [35] conducted

cavitation studies with water temperature changes ranging from 0 to 90°C. It is found from the result that the increase in temperature causes the rise in the cavitation problem.

The cavitation number is known to affect the reference pressure. The formation of cavitation bubbles becomes very destructive when the cavitation number is high. This theory is founded in the previous studies indicating that P_v, σ, L, and ρ_v serve roles as the primary physical properties that induce cavitation [24]. If cavitation is characterized as a decrease in the underwater vapor pressure of the environment, then the ratio of water vapor pressure becomes inversely proportional. The lower the ratio, the more violent the cavitation bubble's inception.

Figure 18 depicts the vapor volume fraction pattern at a ratio of 0.4. The red area denotes the low-pressure contour indicating cavitation bubbles are formed. It can be found in all cases that the lower pressure contours of the propeller rise with increasing temperature. In cavitation with variable temperature, vapor density plays an important part. Water viscosity has a minor effect on the change in Reynolds number, but it significantly impacts the temperature distribution [35]. To illustrate the cavitation phenomenon in more detail, Figure 19 compares pressure contours on the suction side with a condition similar to Figure 18. From the comparison of pressure contour in Figure 19, it can be found that cavitation initiation occurs in the blue area, which represents low-pressure zones. In contrast, the red color represents areas with a higher vapor fraction. It can be summarized that the pressure contour on the suction side is related to cavitation initiation. According to the concept of cavitation, cavitation bubbles will form in environments where the local pressure is smaller than the saturated pressure of water.

6 Concluding remarks

This work investigated the complete and detailed CFD procedures to discuss the cavitation phenomenon of the three-dimensional propeller under various operating conditions. To examine the cavitation phenomena on the (PPTC1) VP1304 propeller model, multiphase problems were formulated using the RANS method with the MRF approach in ANSYS CFX 19 software. The initial study is first conducted for validation purposes. In this case, the numerical result of propeller performances is compared with the data of experimental test using Zwart and Kunz cavitation models with K–ε dan SST turbulence models under various operating conditions. The prediction is that the SST turbulence model has a reasonably good agreement that produces a more reliable result than the K–ε turbulence model.

Based on the simulation result, the following conclusions are summarized:

1. Cavitation increased similarly with the temperature increase, while cavitation inhibited the formation of cavitation bubbles at low temperatures. The comparative data show that the most severe cavitation problem exists in Case 1.
2. Dependent on the various physical properties of water such as the water vapor pressure (P_v), vapor density (ρ_v), latent heat (L), and surface tension (σ), all played essential roles in the rate of cavitation formation.
3. The Rayleigh–Plesset equation can be used to model cavitation and provide a general overview of the results of various physical properties of water.

Based on these investigations, it is considered that this research might be turned into a topic for future work. One alternative that might be pursued is numerical research using compressible cavitation models with a mass transfer that does not occur instantly. To get relevant to the actual phenomenon, an unstable simulation should be executed. Also, an experimental cavitation test is another option that needs to be performed in future work.

Acknowledgements: This work was supported by the RKAT PTNBH Universitas Sebelas Maret – Year 2022, under Research Scheme of "Penelitian Unggulan Terapan" (PUT-UNS), with Research Grant/Contract No. 254/UN27.22/PT.01.03/2022. The support is gratefully acknowledged by the authors.

Author contributions: Conceptualization: M.Y., A.R.P., and A.F.; methodology: M.Y., A.R.P., S.H., and I.Y.; software: M.Y., A.R.P., T.T., and I.Y.; validation: A.R.P., S.H., I.Y., T.M., and F.B.L.; formal analysis: M.Y., A.R.P., T.T., and A.F.; investigation: M.Y., A.R.P., I.Y., T.M., and F.B.L.; resources: A.R.P., S.H., and I.Y.; data curation: M.Y. and A.R.P.; writing – original draft preparation: M.Y. and A.R.P.; writing – review and editing: M.Y., A.R.P., T.T., and A.F.; visualization: A.R.P. and T.T.; supervision: A.R.P.; project administration: A.R.P.; funding acquisition: A.R.P.

Conflict of interest: Authors state no conflict of interest.

References

[1] ICS. Shipping and world trade: driving prosperity; 2017. https://www.ics-shipping.org/shipping-fact/shipping-and-world-trade-driving-prosperity.

[2] Prabowo AR, Bae DM, Sohn JM, Zakki AF, Cao B. Rapid prediction of damage on a struck ship accounting for side impact scenario models. Open Eng. 2017;7(1):91–9.

[3] Prabowo AR, Muttaqie T, Sohn JM, Bae DM. Nonlinear analysis of inter-island RoRo under impact: effects of selected collision's parameters on the crashworthy double-side structures. J Braz Soc Mech Sci Eng. 2018;40(5):248.

[4] Prabowo AR, Cahyono SI, Sohn JM. Crashworthiness assessment of thin-walled double bottom tanker: a variety of ship grounding incidents. Theor Appl Mech Lett. 2019;9(5):320–7.

[5] Prabowo AR, Laksono FB, Sohn JM. Investigation of structural performance subjected to impact loading using finite element approach: case of ship-container collision. Curved Layer Struct. 2020;7(1):17–28.

[6] IMO. Reduction of greenhouse gas emissions from ships – third IMO GHG study 2014 – final report MEPC 67/INF.3; 2014. https://www.imo.org/en/OurWork/Environment/Pages/Greenhouse-Gas-Studies-2014.aspx.

[7] Lindstad H, Asbjørnslett B, Strømman A. The importance of economies of scale for reductions in greenhouse gas emissions from shipping. Energy Policy. 2012;46:386–98.

[8] COP21. Paris agreement; 2015. https://unfccc.int/process-and-meetings/the-paris-agreement/the-paris-agreement

[9] IMO. Ship energy efficiency management plan (SEEMP) for all ships at MEPC 62; 2011. https://www.imo.org/en/OurWork/Environment/Pages/Technical-and-Operational-Measures.aspx.

[10] Yan X, Sun X, Yin Q. Multiparameter sensitivity analysis of operational energy consumption for inland river ships based on backpropagation neural network method. Mar Technol Soc J. 2015;49:148–53.

[11] Wang K, Yan X, Yuan Y, Li F. Real-time optimization of ship energy consumption based on the prediction technology of working condition. Transp Res Part D Transp Environ. 2016;4:81–93.

[12] Andersson H, Fagerholt K, Hobbesland K. Integrated maritime fleet deployment and speed optimization: case study from RoRo shipping. Comput Oper Res. 2015;55(7):233–40.

[13] Zhao F, Yang W, Tan WW, Yu W, Yang J, Chou SK. Power management of vessel propulsion system for thrust efficiency and emissions mitigation. Appl Energy. 2016;161(7):124–32.

[14] Yilmaz N, Dong X, Aktas B, Yang C, Atlar M, Fitzsimmons PA. Experimental and numerical investigations of tip vortex cavitation for the propeller of a research vessel, "The Princess Royal." Ocean Eng. 2020;215:107881.

[15] Lee YW, Yang CY, Chow YC. Evaluations of the outcome variability of RANS simulations for marine propellers due to tunable parameters of cavitation models. Ocean Eng. 2021;226:108805.

[16] Kitagawa H. The Northern Sea Route – the shortest sea route linking East Asia and Europe. Tokyo, Japan: Ship & Ocean Foundation; 2000.

[17] Liu M, Kronback J. The potential economic viability of using the Northern Sea Route as an alternative route Asia and Europe. J Transp Geogr. 2010;18:434–44.

[18] Pruyn JF. Will the Northern Sea Route ever be a viable alternative? Marit Policy Manag. 2016;43(6):661–75.

[19] Theocharis D. Approaches of the profitability of Arctic shipping in the literature. In: Lasserre F, Faury O, editors. Arctic shipping: climate change, commercial traffic and port development. Routledge; 2020. p. 23–39.

[20] Peters A, Lantermann U, el Moctar O. Numerical prediction of cavitation erosion on a ship propeller in model- and full-scale. Wear. 2018;408–409:1–12.

[21] Gugulothu SK. Computational modeling on supercavitating flow over axisymmetric cavitators. Ocean Eng. 2020;210:107515.

[22] Noack JA, Vogel A. Single-shot spatially resolved characterization of laser-induced shock waves in water. Appl Opt. 1998;37(19):4092–9.

[23] Morgut M, Nobile E. Numerical predictions of cavitating flow around model scale propellers by CFD and advance model calibration. Int J Rotat Mach. 2012;2012:618180.

[24] Helal MM, Ahmed TM, Banawan AA, Kotb MA. Numerical prediction of sheet cavitation on marine propellers using CFD simulation with transition-sensitive turbulence model. Alex Eng J. 2018;57(4):3805–15.

[25] Kunz RF, Boger DA, Stinebring DR, Chyczewski TS, Gibeling HJ, Venkateswaran S, Govindan TR. A preconditioned Navier-Stokes method for two-phase flows with application to cavitation prediction. Proceedings of the 14th Computational Fluid Dynamics Conference, Norfolk, VA, USA. 29; 1999. p. 676–88.

[26] Zwart PJ, Gerber AG, Belamri TA. Two-phase flow model for predicting cavitation dynamics. Proceeding of the International Conference on Multiphase Flow, Yokohama, Japan; 2004. p. 559–63.

[27] Lindstad H, Bright RM, Strømman AH. Economic savings linked to future Arctic shipping trade are at odds with climate change mitigation. Transp Policy. 2016;45:24–30.

[28] Furuichi M, Otsuka N. Cost analysis of the Northern Sea Route (NSR) and the conventional route shipping. Proceedings of the IAME 2013 Conference. Marseille; 2013. p. 1–22.

[29] National Snow and Seaice Data Centre Boulder. Total seaice extent in March 2012; 2012. http://nsidc.org/arcticseaseaicenews.

[30] Science Learning Hub. Sea surface temperature; 2001. https://scienceelearn.org.nz.

[31] IOC, SCOR and IAPSO, The international thermodynamic equation of seawater – 2010: calculation and use of thermodynamic properties. Intergovernmental Oceanographic Commission, Manuals and Guides No. 56, UNESCO; 2010.

[32] Millero FJ, Feistel R, Wright DG, McDougall TJ. The composition of standard seawater and the definition of the reference composition salinity scale. Deep Sea Res Part I Oceanogr Res Pap. 2008;55:50–72.

[33] Veronis G. On properties of sea water defined by temperature, salinity and pressure. J Mar Res. 1972;30(2):227–55.

[34] ITTC. Freshwater and seawater properties. ITTC – recommended procedures; 2011. www.ittc.info.

[35] Plesset MS. Temperature effects in cavitation damage. J Fluids Eng. 1972;94(3):559–63.

[36] Al-Arabi AS. Effect of water temperature on centrifugal pumps performance under cavitating and non-cavitating conditions. Proceeding of 8th Internal Conference on Sustainable Energy Technologies, Seoul, Korea; 2008. p. 1–7.

[37] Dular M, Coutier-Delgosha O. Thermodynamic effects during the growth and collapse of a single cavitation bubble. J Fluid Mech. 2013;736:44–66.
[38] Tanaka T. Thermodynamic effect and cavitation performance of a cavitating centrifugal pump. Proceeding of 7th International Symposium on Pumping Machinery, Hamamatsu, Japan; 2011. p. 135–43.
[39] Kim J, Song J. Measurement of temperature effects on cavitation in a turbopump inducer. J Fluids Eng. 2015;138(1):011304.
[40] Yusvika M, Prabowo AR, Tjahjana DDDP, Sohn JM. Cavitation prediction of ship propeller based on temperature and fluid properties of water. J Mar Sci Eng. 2020;8:465.
[41] ANSYS. ANSYS CFX-solver theory guide. ANSYS Inc; 2009. www.ansys.com.
[42] Chen TR, Wang GY, Huang B, Li DQ, Ma XJ, Li XL. Effects of physical properties on thermo-fluids cavitating flows. J Phys Conf Ser. 2015;656:012181.
[43] Lubke L. Potsdam propeller test case (PPTC) cavitation in oblique flow case 2. Proceeding of The fourth International Symposium on Marine Propulsors; 2015.
[44] Morgut M, Nobile E, Jost D, Skerlavaj A. Numerical prediction of the PPTC propeller in oblique flow. Proceeding of 4th International Symposium on Marine Propulsors. Austin, Texas; 2015. p. 138–42.
[45] Hosien MA, Selim SM. Experimental and theoretical investigation on the effect of pumped water temperature on cavitation breakdown in centrifugal pumps. J Appl Fluid Mech. 2017;10:1079–89.
[46] Dular M, Petkovšek M. Cavitation erosion in liquid nitrogen. Wear. 2018;400–401:111–8.